Research Square

Preprints are preliminary reports that have not undergone peer review.
They should not be considered conclusive, used to inform clinical practice,
or referenced by the media as validated information.

Parity-selective tuning of higher-order mode nonlinearities in a doubly clamped MEMS beam resonator

Chao Li
Tokyo University of Agriculture and Technology
Xiaojian Xiang
Research Institute of Tsinghua University in Shenzhen
Zihao Zhao
Tokyo University of Agriculture and Technology
Qian Liu
Tokyo University of Agriculture and Technology
Ya Zhang
zhangya@go.tuat.ac.jp
Tokyo University of Agriculture and Technology

Research Article

Keywords:

Posted Date: November 20th, 2026

DOI: https://doi.org/10.21203/rs.3.rs-11550498/v1

License: This work is licensed under a Creative Commons Attribution 4.0 International License.
Read Full License

Additional Declarations: No competing interests reported.

Parity-selective tuning of higher-order mode nonlinearities in a doubly clamped MEMS beam resonator

Chao Li[1,2], Xiaojian Xiang[2], Zihao Zhao[1], Qian Liu[1] and Ya Zhang[1a)]

[1]Institute of Engineering, Tokyo University of Agriculture and Technology, Koganei-shi, Tokyo, 184-8588, Japan

[2]Institute of Superlubricity Technology, Research Institute of Tsinghua University in Shenzhen, Shenzhen, China

[a)] Electronic mail: zhangya@go.tuat.ac.jp

Abstract

Strain tuning can suppress or reverse the fundamental mode nonlinearity of microelectromechanical-system (MEMS) resonators. Extending this control to higher-order modes requires understanding its mode dependence. Here, we demonstrate a parity-selection rule for mode-selective nonlinear tuning in an initially curved, doubly clamped GaAs beam resonator. The nonlinear model shows that the curvature-induced quadratic nonlinearity depends on a modal overlap between the initial beam profile and the vibration mode shape. The overlap vanishes when these two profiles have opposite parity about the beam midpoint, whereas matching parity allows quadratic softening to compete with cubic hardening. Measurements of the first four out-of-plane bending modes under thermal strain tuning reproduce the grouping predicted for an even-parity initial profile. The first and third modes undergo hardening-to-softening transitions, whereas the second and fourth remain hardening over the measured heating-power range. Further calculations predict that an odd-parity initial profile enables such transitions in the second and fourth modes. These results provide a symmetry-based design guideline for mode-selective suppression and reversal of nonlinear frequency shifts.

I. Introduction

Microelectromechanical-system (MEMS) resonators [1-3] are widely used as frequency-shift transducers for mass sensing [4,5], biological and chemical detection [6], and radiation detection [7-10]. Beyond single-mode operation, the use of multiple vibrational modes is increasingly attractive. The higher modes provide additional sensing channels and capability to discriminate different perturbations, while also supporting nonlinear modal dynamics including dispersive coupling, coherent internal resonance, and mechanical frequency comb generation [11-15]. In sensing applications, large oscillation amplitudes can improve readout robustness and signal-to-noise ratio. Increasing the amplitude, however, can also drive the resonator into the nonlinear regime, where the resonance frequency becomes amplitude dependent and hysteretic responses may emerge [16-20]. Predicting and controlling the nonlinear response of individual modes is therefore important both for maintaining stable sensing operation and for exploiting the nonlinear dynamics of higher-order modes.

Strain engineering provides an effective route to controlling the magnitude and sign of mechanical nonlinearity in micro- and nanomechanical beam resonators [21–24]. In GaAs doubly clamped MEMS beams, thermally induced strain and preloaded lattice-mismatch strain have been used to suppress and reverse fundamental-mode nonlinearity [22,23]. This control relies on the competition between cubic hardening and a softening contribution arising from quadratic nonlinearity caused by the initial curvature of the beam. Complementary studies on geometry and shape optimization have demonstrated that beam shape can also be used to tailor nonlinear modal responses [25-27]. These developments establish strain and beam shape as key design parameters for controlling mechanical nonlinearity.

In this paper, we demonstrate a parity-selection rule for nonlinearity tuning of higher-order modes in an initially curved, doubly clamped GaAs beam resonator. The model identifies the parity-dependent modal overlap between the initial beam profile and the vibration mode shape as the key factor governing the quadratic softening contribution. Measurements of the first four out-

of-plane bending modes under thermal strain tuning reproduce the grouping predicted for an even-parity initial profile. The first and third modes undergo hardening-to-softening transitions in their nonlinearities, whereas the second and fourth remain hardening over the measured heating-power range. Numerical calculations further show that an odd-parity initial profile enables such transitions in the second and fourth modes. Together, these results establish initial-shape parity as a design parameter for mode-selective suppression and reversal of nonlinear frequency shifts.

II. Theoretical model and parity selection rule

We consider an initially curved doubly clamped MEMS beam, as depicted in Fig. 1(a). The initial curvature is described by a transverse displacement as [28],

$$X_0(u) = x_0\phi_0(u) = -\frac{x_0}{2}\left(1 - \cos\frac{2\pi}{L}u\right), \tag{1}$$

where x_0 is the initial center deflection, $\phi_0(u)$ is the profile function of initial shape; u is the coordinate along the beam length (L). During vibration, the dynamic displacement from the equilibrium position is written as

$$X(u,t) = x_n(t)\phi_n(u), \tag{2}$$

where $x_n(t)$ and $\phi_n(u)$ represent the modal displacement and the mode shape function of the nth bending mode, respectively. We start from the Euler-Bernoulli beam equation with the initial curvature and the vibration-induced tension change, the nonlinear motion for the nth mode can be written in the Duffing form (more details are presented in Appendix A), as

$$\ddot{x}_n + \omega_n^2 x_n + \alpha_n x_n^3 + \beta_n x_n^2 = 0, \tag{3}$$

in which ω_n is the natural angular frequency of the nth mode, α_n is the cubic coefficient that gives hardening contribution, and β_n is the quadratic coefficient that gives softening contribution. The coefficients α_n and β_n lead to nonlinear oscillations that manifest as amplitude-dependent frequency shifts ($\Delta\omega_n$), which can be described as

$$\Delta\omega_n = \omega_n\left(\frac{3\alpha_n}{8\omega_n^2} - \frac{\beta_n^2}{2\omega_n^4}\right)A_n^2, \tag{4}$$

where A_n is the oscillation amplitude, and $Y_T = \frac{3\alpha_n}{8\omega_n^2} - \frac{\beta_n^2}{2\omega_n^4}$ is the total nonlinearity coefficient of the nth mode. A positive Y_T corresponds to hardening behavior, in which the resonance frequency shifts toward higher frequency side with increasing oscillation amplitude, while a negative Y_T corresponds to softening behavior. The expression of Y_T indicates that the total nonlinearity is governed by a competition between α_n and β_n, and it changes sign only when the β_n becomes sufficiently strong to compensate the α_n. The important point is that α_n is a constant for a given vibration mode, whereas β_n is proportional to the modal overlapping parameter (W_{0n}) between the initial mode shape (ϕ_0) and the vibration mode shape(ϕ_n), which can be calculated as

$$W_{0n} = \int_0^1 \frac{\partial \phi_0}{\partial u} \frac{\partial \phi_n}{\partial u} du. \quad (5)$$

As seen, this W_{0n} appears only when the ϕ_0 and the ϕ_n have a nonzero mode-shape overlap. If the two shapes have opposite parity, the overlap integral vanishes or is strongly suppressed ($W_{0n} \approx 0$), and the quadratic softening channel is not activated. In contrast, when they have the same parity, W_{0n} becomes finite and the quadratic term can compensate the cubic hardening term. This parity dependence is the origin of the mode-selective tunability discussed in this study.

III. Tunability prediction of parity-selective mode groups

For the initial shape used in the present device, ϕ_0 has even parity with respect to the beam center, as shown in Fig. 1, which plots the assumed initial beam shape together with the one-dimensional profiles of the first four bending modes. The 1st and 3rd out-of-plane bending modes have the same parity as this initial shape, whereas the 2nd and 4th bending modes have the opposite parity. The model therefore predicts two distinct groups. For the 1st and 3rd modes, $W_{0n} \neq 0$, so the quadratic softening contribution can be enhanced by strain and may drive Y_T from positive to negative. For the 2nd and 4th modes, $W_{0n} \approx 0$, so the quadratic softening contribution is absent or strongly suppressed, and the nonlinear response should remain dominated by cubic hardening.

We next evaluate how the parity-selection rule appears in specific higher-order modes of the present device by numerical analysis. The calculation was performed for a doubly clamped GaAs MEMS beam resonator with dimensions of 133 μm (L) × 27 μm (b) × 1 μm (h). The Young's modulus and mass density were taken as E = 85.9 GPa and ρ = 5307 kg/m^3, respectively. An initial curvature with a normalized center deflection of x_0/h=0.1 was assumed. The mode shape functions of the first four bending modes were adopt from the standard solution for a doubly clamped beam [17], as

$$\phi_1 = 1.01781\,cos[4.73004u] - 1.01781\,cosh[4.73004u] - sin[4.73004u] + sinh[4.73004u], \quad (6)$$

$$\phi_2 = 0.999223\,cos[7.8532u] - 0.999223\,cosh[7.8532u] - - sin[7.8532u] + sinh[7.8532u], \quad (7)$$

$$\phi_3 = 1.00003cos[10.9956u] - 1.00003\,cosh[10.9956u] - sin[10.9956u] + sinh[10.9956u], \quad (8)$$

$$\phi_4 = 0.999999\,cos[14.1372u] - 0.999999\,cosh[14.1372u] - - sin[14.1372u] + sinh[14.1372u]. \quad (9)$$

A compressive strain along the beam axis, ε, was employed to tune the nonlinearity of each mode as it is coupled with the parameters β_n and ω_n in the expression of Y_T (see more details in Appendix A). This strain is introduced thermally in the subsequent experiment.

Figure 2 shows the calculated Y_T, as a function of ε for the four modes. For the 1st bending mode [Fig. 2(a)] and the 3rd bending mode [Fig. 2(c)], Y_T is positive at small compressive strain, corresponding to hardening behavior. As ε increases, however, Y_T decreases markedly and changes sign in the calculated trend. This sign reversal indicates that the strain-enhanced quadratic softening contribution can compensate, and then exceed, the cubic hardening contribution. In addition, the transition from positive to negative Y_T indicates a strain region near Y_T =0, where the amplitude-dependent frequency shift is expected to be strongly reduced.

The 2nd and 4th bending modes behave differently. As shown in Figs. 2(b) and 2(d), Y_T remains positive over the calculated strain range for both modes. In these opposite-parity modes, the quadratic softening channel is absent in the present even-parity beam configuration, so increasing compressive strain does not produce a hardening-to-softening transition. Their response instead remains governed by the cubic hardening term, and the resonance frequency is expected to shift to higher frequency side with increasing oscillation amplitude.

The numerical results therefore confirm a parity-dependent grouping of the first four bending modes and convert the parity-selection rule into an experimentally testable prediction. Under thermal strain tuning in the experiment, modes with the same parity as the initial shape can acquire a strain-enhanced quadratic softening contribution and can be tuned through a zero-nonlinearity region into softening behavior. Modes with the opposite parity remain hardening because the relevant overlap with the initial shape is suppressed.

IV. Device and measurement method

Figure 3(a) shows a microscope image of the fabricated doubly clamped MEMS beam resonator used in this work, whose geometric dimensions are the same as those used in the numerical analysis. The device was fabricated using essentially the same wafer structure and microfabrication procedures as those reported in our previous studies on GaAs-based doubly clamped MEMS beam resonators [11,22]. Therefore, the fabrication details are not repeated here. Briefly, the suspended beam structure was formed from a modulation-doped (Al,Ga)As/GaAs heterostructure, and top metal gates (C_1 and C_2) were patterned on the beam to drive its mechanical vibration through the piezoelectric effect of GaAs. A thin NiCr layer was also deposited on the beam, which can be used as a heater for introducing thermal strain in the beam. It is noted that, owing to the existence of mesa structure, the beam generally has an initial deflection rather than being perfectly straight [23], as shown in Fig. 1.

The experimental setup is schematically shown in Fig. 3(b). An ac voltage, V_D, was applied to one of the piezoelectric capacitors to excite the beam, and the resulting mechanical vibration was measured by a laser Doppler vibrometer together with a lock-in amplifier. In the present work, a broad sweep was first carried out under a weak-drive condition, as shown in Fig. 3(c), in order to identify the natural resonance frequencies ($f=\omega_n/2\pi$) of the first four bending modes used for the subsequent nonlinear characterization. Their natural resonance frequencies are 240 kHz, 652 kHz, 1275 kHz, and 2070 kHz, respectively. After the target modes were identified, each mode was then individually measured in a narrow frequency window around its own resonance frequency under different driving-voltage levels, which allowed us to accurately track the resonance-frequency shift induced by increasing amplitude.

Representative examples of the nonlinearity measurements are shown in Figs. 4(a) and 4(b) for the 1st and 2nd bending modes. Without heating, the resonance spectra of each mode were recorded at different driving-voltage levels, so that the intrinsic nonlinear response of the mode could be characterized. As the driving level increased, the oscillation amplitude increased and the resonance peak gradually shifted in frequency, indicating the transition into the nonlinear regime. By comparing the frequency corresponding to the peak position (f') at each drive level with the natural resonance frequency obtained under weak excitation, the frequency drift, Δf ($\Delta f=f'-f$), of the mode was extracted. Meanwhile, the oscillation amplitude, A_n, of the corresponding mode was obtained from the measured vibration response. Following Eq. (4), these two experimentally accessible quantities were then used to determine the nonlinear coefficient of each mode. Therefore, by plotting the measured Δf as a function of a_n^2, the value of Y_T can be obtained from a linear fitting. A positive fitted Y_T corresponds to hardening behavior ($\Delta f>0$), whereas a negative fitted Y_T indicates softening behavior ($\Delta f<0$). This fitting method is also used for the nonlinearity characterization of each mode under different thermal condition.

In this work, thermal strain was introduced into the MEMS beam by applying a dc voltage, (V_{NiCr}) to the NiCr heater [see Fig. 3(a)]. Figs. 4 (c) and 4(d) show the resonance spectra of the 1st

and 2nd bending modes under three specific thermal conditions, respectively. As the heating power, P, increased, both the natural resonance frequency and the nonlinearity of the 1st bending mode were tuned. In particular, Figs. 4 (c) shows a clear transition in the resonance spectra of the 1st bending mode from hardening to linear and then to softening. Such a clear transition did not occur in the resonance spectra of the 2nd bending mode, which primarily exhibits frequency tuning. To characterize these tuning behaviors in detail, we measured the resonance spectra of each mode at various heating powers and then extracted the corresponding Y_T from the fitting procedure described above. The measured Δf and fitted Y_T are used to test whether the parity-dependent grouping predicted by the numerical calculation is observed experimentally.

V. Experimental verification of parity-selective tuning rule

Figure 5 summarizes the amplitude-dependent frequency shift and the fitted total nonlinearity coefficient for the first four bending modes at various heating powers. The left panels [Figs. 5(a), 5(c), 5(e), and 5(g)] show the measured Δf-amplitude relations, and the right panels [Figs. 5(b), 5(d), 5(f), and 5(h)] summarize the extracted Y_T values together with the natural resonance frequencies. The core question is whether the same-parity modes, namely the 1st and 3rd bending modes, show a hardening-to-softening transition, whereas the opposite-parity modes, namely the 2nd and 4th bending modes, remain hardening.

The 1st and 3rd bending modes exhibit the predicted tunable behavior. For the 1st bending mode, the Δf-amplitude curves in Fig. 5(a) evolve from positive frequency shifts at low heating power to negative frequency shifts at higher heating power. The corresponding Y_T values in Fig. 5(b) first remain positive and then decrease rapidly to negative values. This polarity reversal indicates that the total nonlinearity is strongly suppressed and then changes from hardening to softening. A similar trend is observed for the 3rd bending mode. As shown in Figs. 5(c) and 5(d), the measured Δf-amplitude curves and the fitted Y_T values also change from hardening to softening as the heating power increases. Thus, the two modes that have the same parity as the initial beam shape both show a thermally induced sign reversal of Y_T.

The frequency tuning measured under weak excitation further supports the variation trend of Y_T. For both the 1st and 3rd modes, the natural resonance frequency decreases with heating power, reaches a minimum, and then increases again [see Figs. 5(b) and 5(d)]. The rapid reduction and sign reversal of Y_T occur in the same heating-power range where the resonance frequency shows this nonmonotonic variation. This correlation indicates that the nonlinear response is strongly affected by the frequency change induced by thermal strain in the static mechanical state of the beam. In the same-parity modes, this frequency change enhances the quadratic softening contribution sufficiently to compensate the cubic hardening contribution.

The 2nd and 4th bending modes provide the contrasting case. For the 2nd mode, the measured Δf-amplitude curves remain positive over the measured heating-power range [Fig. 5(e)], and the fitted Y_T values remain positive in Fig. 5(f). Although the natural resonance frequency decreases and then tends to plateau with heating power, no polarity reversal of Y_T is observed. The 4th bending mode shows the same behavior [see Fig. 5(g) and 5(h)]. Therefore, thermal tuning modifies the resonance frequencies of these two modes but does not drive their nonlinear response into a softening regime.

It is noted that, thermal power is used as an experimental tuning knob, whereas the numerical analysis uses compressive strain. Together with possible effects from the actual initial shape, residual stress, and boundary imperfections, this difference may lead to small quantitative deviations between the experimental and theoretical values of Y_T. However, it does not affect the parity-based mode grouping and the overall trend of Y_T.

The experimental results reproduce the parity-dependent grouping predicted by the model and confirm the parity-selection rule again. Although all the four modes experience thermal tuning, only the modes whose parity matches that of the initial beam shape exhibit a zero crossing of Y_T. The 1st and 3rd modes evolve from hardening to softening, whereas the 2nd and 4th modes remain positive over the entire heating range.

VI. Design rule: selecting tunable modes by initial shape engineering

The parity-selection rule can be used not only to explain the measured mode grouping, but also to design which higher-order modes will be tunable. The key design parameter is the parity of the initial beam shape. Once the initial profile is chosen, the modes with parity-allowed overlap ($W_{0n} \neq 0$) are expected to acquire the quadratic softening contribution and become candidates for zero-nonlinearity or softening operation, whereas modes with suppressed overlap ($W_{0n} \approx 0$) remain hardening. Thus, mode-selective nonlinearity tuning can be realized by designing the initial beam profile.

To demonstrate this design rule, we numerically consider an initial beam shape with odd parity. Such an initial profile can be viewed as a shape-engineered counterpart to the even-parity initial shape used in the present device, and related curved-beam shape engineering has been discussed in recent work [27]. In this case, the assumed initial shape is described as

$$\phi_0(u) = -\frac{1}{2}\sin\left(\frac{2\pi}{L}u\right)\left(1 - \cos\frac{2\pi}{L}u\right). \tag{10}$$

For this odd-parity initial shape, the W_{0n} becomes finite for modes with the corresponding parity and suppressed for modes with the opposite parity. Using the same numerical procedure, we calculated the Y_T for the 2nd and 4th bending modes under this odd-parity initial-shape condition. The results are shown in Figs. 6(a) and 6(b), respectively. In contrast to the even-parity case shown in Fig. 2, both the two modes now show a transition from positive to negative Y_T as the compressive strain is increased. This calculated sign reversal indicates that changing the initial-shape parity can activate the quadratic softening contribution in modes that previously remained hardening.

This numerical test extends the parity-selection rule from an explanation of the present experiment to a mode-selection guideline. In the present even-parity beam, the 1st and 3rd modes are the tunable modes, whereas the 2nd and 4th modes remain hardening. If the initial beam shape is engineered with the opposite parity, the tunable set can in principle be shifted to the 2nd and 4th

modes. Thus, initial-shape parity engineering suggests a route toward mode-selective control of nonlinearity in doubly clamped MEMS beam resonators.

Such mode-selective control may be useful when a particular higher-order mode is preferred for sensing, multimode operation, or tailored nonlinear response. Modes that can be tuned near $Y_T = 0$ are expected to show reduced amplitude-dependent frequency shifts, which is favorable for large-amplitude operation with improved frequency stability. At the same time, modes that remain hardening can also be selected when a stable positive nonlinearity is desirable. The parity-selection rule therefore provides a physical guideline for designing nonlinear response mode by mode, rather than treating strain tuning as a uniform effect applied to all resonances.

VII. Conclusion

In conclusion, we have investigated the parity-dependent nonlinear response of an initially curved doubly clamped GaAs MEMS beam resonator under thermal strain tuning. By combining a nonlinear beam model, numerical calculations, and measurements of the first four out-of-plane bending modes, we show that nonlinearity tunability of modes is governed by the parity relation between the vibrational mode and the initial beam shape.

For the present even-parity initial shape, the 1st and 3rd bending modes have the same parity with the initial beam profile. These modes acquire a quadratic softening contribution that can compensate the cubic hardening contribution, leading to a transition from hardening to softening as the thermal strain is increased. In contrast, the 2nd and 4th bending modes have the opposite parity to the initial shape. Their quadratic softening channel is suppressed, and their nonlinear response remains dominated by cubic hardening over the measured heating-power range.

The experimental results agree with the numerical prediction and separate the four modes into the same two parity-dependent groups. This agreement clarifies why thermal strain tuning does not simply change the nonlinearity of all modes in the same way, but instead selectively drives parity-allowed modes toward quasi-zero nonlinearity or into the softening regime.

The design calculation with an odd-parity initial shape further suggests that the set of tunable modes can be selected by engineering the initial beam profile. This result elevates the observed parity-dependent tunable modes grouping from a device-specific phenomenon to a general parity-based design rule. Initial-shape parity engineering therefore provides a practical route toward mode-selective control of nonlinearity in doubly clamped MEMS beam resonators, which may be useful for systems requiring reduced amplitude-dependent frequency shifts, large-amplitude operation, or tailored nonlinear response.

Appendix A. Derivation details for the modal equation

Given by the initial x_0, the motion equation of the MEMS beam describing its transverse vibrations during the oscillation can be described as,

$$\rho S \frac{\partial^2 X}{\partial t^2} = -EI\left(\frac{\partial^4 X}{\partial u^4} + \frac{d^4 X_0}{du^2}\right) + T\left(\frac{\partial^2 X}{\partial u^2} + \frac{d^2 X_0}{du^2}\right), \quad \text{(A1)}$$

with the following boundary conditions:

$$X|_{u=0,L} = 0 \text{ and} \frac{\partial X}{\partial u}\Big|_{u=0,L} = 0, \quad \text{(A2)}$$

where t is the time scale; ρ is the density; E is the Young's modulus; S and I denote the cross-section area and the moment of inertia ($S=bh$ and $I=bh^3/12$ for beams of rectangular cross-sections, with b and h being the width and thickness of the MEMS beam, respectively); T is the tension in the MEMS beam ($T= T_0+\Delta T$), consisting of its inherent tension T_0 and the additional tension ΔT coming from the extension of the beam length (ΔL) in vibrations.

We start from Eq.(A1), in which the T is composed of the T_0 and ΔT. T_0 is a constant, and the ΔT here is calculated as

$$\Delta T = ES\frac{\Delta L}{L} = \frac{ES}{2L}\int_0^L \left[\left(\frac{\partial X}{\partial u}\right)^2 + 2\frac{\partial X}{\partial u}\frac{dX_0}{du}\right] du. \quad \text{(A3)}$$

Decomposing $X(u,t)$ into $\phi_n(u)$ and $x_n(t)$, and together with Eqs.(A3) and (1) to substitute into Eq. (A1), yields

$$\rho S\phi_n \frac{\partial^2 x_n}{\partial t^2} = -EI\left(x_n \frac{\partial^4 \phi_n}{\partial u^4} + x_0 \frac{\partial^4 \phi_0}{\partial u^4}\right) + \left(x_n \frac{\partial^2 \phi_n}{\partial u^2} + x_0 \frac{d^2 \phi_0}{du^2}\right)\left(T_0 + \frac{ES}{2L}\int_0^L \left[\left(x_n \frac{\partial n}{\partial u}\right)^2 + 2x_0 x_n \frac{\partial \phi_n}{\partial u}\frac{\partial \phi_0}{\partial u}\right] du\right). \quad \text{(A4)}$$

We multiply $\phi_n(u)$ to both sides of Eq.(A4) and then integrate it over beam length (L). Since the whole equation is complex, we here process it one by one. Following the orthonormality for flexural modes of a beam: $\int_0^L \phi_j \phi_k du = L\ (j = k)$, and using $\frac{\partial^4 \phi_n}{\partial u^4} = \frac{\psi_n^4}{L^4}\phi_n$. The term to the left of the equal sign can be expressed as

$$\int_0^L \rho S\phi_n \frac{\partial^2 x_n}{\partial t^2}\phi_n du = \rho SL\ddot{x}_n. \quad \text{(A5)}$$

The first term to the right of the equal sign can be expressed as

$$\int_0^L -\phi_n EI\left(x_n \frac{\partial^4 \phi_n}{\partial u^4} du + x_0 \frac{\partial^4 \phi_0}{\partial u^4}\right) = -\frac{EI\psi_n^4}{L^3}x_n + \frac{EI\psi_0^4}{L^4}x_0 \int_0^1 \phi_0 \phi_n du. \quad \text{(A6)}$$

where $\psi_n = \{4.73,\ 7.8532,\ 10.996,\ 14.1372,\ \ldots\}$ for n=0/1,2,3,4…. To be cautious, here we decompose the remaining parenthesized multiplication term into four terms, and process them one by one. Using integration by parts, the two terms containing T_0 can be simplified as follows

$$\int_0^L x_n T_0 \phi_n \frac{\partial^2 \phi_n}{\partial u^2} du = T_0 x_n\left(-\int_0^L \frac{\partial \phi_n}{\partial u}\frac{\partial \phi_n}{\partial u} du + \phi_n \frac{\partial \phi_n}{\partial u}\Big|_{(0,L)}\right) = -\frac{T_0}{L}x_n W_{nn}, \quad \text{(A7)}$$

$$\int_0^L x_0 T_0 \phi_n \frac{\partial^2 \phi_0}{\partial u^2} du = T_0 x_0\left(-\int_0^L \frac{\partial \phi_0}{\partial u}\frac{\partial \phi_n}{\partial u} du + \phi_n \frac{\partial \phi_0}{\partial u}\Big|_{(0,L)}\right) = -\frac{T_0}{L}x_0 W_{0n}, \quad \text{(A8)}$$

where $\phi_n \frac{\partial \phi_n}{\partial u}\Big|_{(0,L]} = \phi_n \frac{\partial \phi_0}{\partial u}\Big|_{(0,L]} = 0$ due to the boundary condition as shown in Eq. (A2), $W_{nn} = \int_0^1 \frac{\partial \phi_n}{\partial u}\frac{\partial \phi_n}{\partial u} du, (n = 1,2,3\cdots)$ and $W_{0n} = \int_0^1 \frac{\partial \phi_0}{\partial u}\frac{\partial \phi_n}{\partial u} du, (n = 1,2,3\cdots)$. W_{nn} represents the modal overlapping parameter between the vibration mode shape(ϕ_{n}) itself. The remaining two terms can be simplified as

$$\frac{x_n W_{nn}}{L} \times \frac{ES}{2L} \times \frac{\left(x_n{}^2 W_{nn} + 2x_0 x_n W_{0n}\right)}{L}. \quad \text{(A9)}$$

$$\frac{x_0 W_{0n}}{L} \times \frac{ES}{2L} \times \frac{\left(x_n{}^2 W_{nn} + 2x_0 x_n W_{0n}\right)}{L}. \quad \text{(A10)}$$

We combine the Eqs.(A5 -(A10) to form

$$\ddot{x}_n + \left(\frac{EI\psi_n^4}{\rho SL^4} + \frac{T_o W_{nn}}{\rho SL^2} + \frac{x_0^2 E}{\rho L^4} W_{0n}^2\right) x_n + \left(\frac{E}{2\rho L^4} W_{nn}^2\right) x_n^3 + \left(\frac{3x_0 E}{2\rho L^4} W_{nn} W_{0n}\right) x_n^2 +$$

$$\frac{EI\psi_0^4}{L^4} x_0 \int_0^1 \phi_0 \phi_n du + \frac{T_0 x_0}{L} W_{0n} = 0. \qquad \text{(A11)}$$

where the last two terms indicate the equilibrium for flexural of rigidity and internal stress, at a steady state. We assume that a compressive strain, ε, is introduced in the beam, then the x_0 will increase to x_T. At the steady-state, the relationship between x_T and x_0 can be expressed as

$$-x_0 \frac{EI\psi_0^4}{L^4} \phi_0 = -x_T \frac{EI\psi_0^4}{L^4} \phi_0 + T_0 x_T \frac{\partial^2 \phi_0}{\partial u^2}. \qquad \text{(A12)}$$

By Form multiplying $\phi_0(u)$ to both sides of Eq. (A12) and then integrate it over beam length. Then we can obtain the expression of x_T, as

$$x_T = \frac{\frac{EI\psi_0^4}{L^4} \int_0^L (\phi_0)^2 du}{\frac{EI\psi_0^4}{L^4} \int_0^L (\phi_0)^2 du + \frac{T_0 W_{00}}{L}} x_0. \qquad \text{(A13)}$$

Note that, here, the inherent tension $T_0=ES\varepsilon_r$ is not equal to the induced compressive load $T=ES\varepsilon$, which is because part of the ε is released by the increase in x_T, and a residual strain, ε_r, is remained, as

$$\varepsilon_r = \varepsilon - \frac{({x_T}^2 - {x_0}^2)}{2L^2} W_{00}. \qquad \text{(A14)}$$

Since the steady-state equation holds for any new equilibrium position caused by the applied ε, the last two terms in Eq.(A11) can be eliminated by replacing x_0 appearing in the other terms with the x_T, and then Eq. (A11) becomes

$$\ddot{x}_n + \left(\frac{EI\psi_n^4}{\rho SL^4} + \frac{T_o W_{nn}}{\rho SL^2} + \frac{x_T^2 E}{\rho L^4} W_{0n}^2\right) x_n + \left(\frac{E}{2\rho L^4} W_{nn}^2\right) x_n^3 + \left(\frac{3x_T E}{2\rho L^4} W_{nn} W_{0n}\right) x_n^2 = 0. \qquad \text{(A15)}$$

By using $\omega_n = \sqrt{\frac{EI\psi_n^4}{\rho SL^4} + \frac{T_o W_{nn}}{\rho SL^2} + \frac{x_T^2 E}{\rho L^4} W_{0n}^2}$, $\alpha_n = \frac{E}{2\rho L^4} W_{nn}^2$ and $\beta_n = \frac{3x_T E}{2\rho L^4} W_{nn} W_{0n}$, Eq.(A15) can be further written in the form of Eq. (3), as

$$\ddot{x}_n + \omega_n^2 x_n + \alpha_n x_n^3 + \beta_n x_n^2 = 0. \qquad \text{(A16)}$$

To further explore how α_n and β_n affect the total nonlinearity, we take a solution for Eq.**Error! Reference source not found.**), as

$$x_n = \frac{1}{2}\left(A_n e^{i\omega_n' t} + \overline{A_n} e^{-i\omega_n' t}\right) + \delta, \quad \text{(A17)}$$

where A_n indicates the oscillation amplitude of nth mode and the overbar indicates the complex conjugate, ω_n' indicates the resonance frequency with the oscillation of the beam for the nth mode, and δ is a perturbed parameter. By substituting Eq. (A17) into Eq. (A16), dropping terms in higher order of δ, and then matching the terms in $e^{i\omega_n' t}$ and constant terms, respectively, this yields the following two equations,

$$\delta\omega_n^2 + \frac{3}{2}\delta\alpha_n A_n^2 + \frac{1}{2}\beta_n A_n^2 = 0. \quad \text{(A18)}$$

$$-{\omega_n'}^2 + \omega_n^2 + \frac{3}{4}\alpha_n A_n^2 + 2\beta_n\delta = 0. \quad \text{(A19)}$$

From Eq.(A18) we can obtain:

$$\delta = -\frac{\frac{1}{2}\beta_n A_n^2}{\omega_n^2 + \frac{3}{2}\delta\alpha_n A_n^2}, \quad \text{(A20)}$$

in which $\frac{3}{2}\delta\alpha_n A_n^2$ can be ignored since it is a much smaller value compared to ω_n^2, the Eq. (A20) thus can be written as

$$\delta = -\frac{\frac{1}{2}\beta_n A_n^2}{\omega_n^2}, \quad \text{(A21)}$$

Substituting Eq. (A21) into Eq. (A19), yields

$${\omega_n'}^2 = \omega_n^2 + \frac{3}{4}\alpha_n A_n^2 - \frac{\beta_n^2 A_n^2}{\omega_n^2}, \quad \text{(A22)}$$

Dividing both sides of Eq. (A22) by ω_n^2, and then taking the square root, yields

$$\frac{\omega_n'}{\omega_n} = \sqrt{1 + \frac{3\alpha_n}{4\omega_n^2}a_n^2 - \frac{\beta_n^2 A_n^2}{\omega_n^4}}, \quad \text{(A23)}$$

We apply Taylor expansion to Eq. (A23) and drop the higher order terms and just remain the first two terms, we can obtain:

$$\omega_n' = \omega_n \left[1 + \left(\frac{3\alpha_n}{8\omega_n^2} - \frac{\beta_n^2}{2\omega_n^4}\right) A_n^2\right], \qquad \text{(A24)}$$

in which $Y_T = \frac{3\alpha_n}{8\omega_n^2} - \frac{\beta_n^2}{2\omega_n^4}$ is the total nonlinearity coefficient of nth mod. Eq.(A24) can be further written as

$$\Delta\omega_n = \omega_n \left(\frac{3\alpha_n}{8\omega_n^2} - \frac{\beta_n^2}{2\omega_n^4}\right) A_n^2, \quad \text{(A25)}$$

where $\Delta\omega_n = \omega_n' - \omega_n$ is the amplitude-dependent frequency shift.

Author contributions

Ya Zhang conceived the idea of the work. Chao Li designed and fabricated the device, and performed the experiments and data analysis. Qian Liu and Zihao Zhao supported the fabrication and measurement. The theoretical works were done by Chao Li. Chao Li and Ya Zhang wrote the manuscript. Xiaojian Xiang gave suggestions for improving the manuscript. All the authors contributed to the discussions in this work.

Funding

This work was financially supported in part by JSPS KAKENHI Grant Numbers 24K00937 and 26K22460, and grant from Murata Science Foundation. The authors (Chao Li and Xiaojian Xiang) wish to acknowledge the support from National Key Research and Development Program of China (Grant No. 2025YFF0513900), National Natural Science Foundation of China (Grant No. 62574138), and Guangdong Special Support Plan Science and Technology Innovation Young Top-notch Talents (Grant No.2023TQ07Z553).

Data availability

The datasets generated during and/or analyzed during the current study are available from the corresponding author upon reasonable request.

Declarations

Conflict of interest The authors have no relevant financial or non-financial interests to disclose.

References

1. Ekinci, K. & Roukes, M. Nanoelectromechanical systems. *Rev. Sci. Instrum.* **76**, 061101 (2005).

2. Boisen, A., Dohn, S., Keller, S. S., Schmid, S. & Tenje, M. Cantilever-like micromechanical sensors. *Rep. Prog. Phys.* **74**, 036101 (2011).

3. Cleland, A. N. *Foundations of Nanomechanics: From Solid-State Theory to Device Applications* (Springer, New York, 2003).

4. Zhao, W. et al. High-order resonance enhancing the mass sensitivity of diamond cantilevers. *APL Mater.* **13**, 041124 (2025).

5. Zhang, T., Wei, X., Jiang, Z. & Cui, T. Sensitivity enhancement of a resonant mass sensor based on internal resonance. *Appl. Phys. Lett.* **113**, 223505 (2018).

6. Eom, K., Park, H. S., Yoon, D. S. & Kwon, T. Nanomechanical resonators and their applications in biological/chemical detection: Nanomechanics principles. *Phys. Rep.* **503**, 115 (2011).

7. Zhang, Y., Hosono, S., Nagai, N., Song, S.-H. & Hirakawa, K. Fast and sensitive bolometric terahertz detection at room temperature through thermomechanical transduction. *J. Appl. Phys.* **125**, 151602 (2019).

8. Qian, Z. et al. Graphene-aluminum nitride NEMS resonant infrared detector. *Microsyst. Nanoeng.* **2**, 16026 (2016).

9. Hui, Y. et al. Plasmonic piezoelectric nanomechanical resonator for spectrally selective infrared sensing. *Nat. Commun.* **7**, 11249 (2016).

10. Froberger, K. et al. SOI-based micro-mechanical terahertz detector operating at room-temperature and atmospheric pressure. *Appl. Phys. Lett.* **120**, 261103 (2022).

11. Li, C. et al. Significant tuning of dispersive mode coupling in doubly clamped MEMS beam resonators using the thermally induced buckling effect. *Phys. Rev. Applied* **23**, 054061 (2025).

12. Niu, T., Nagai, N., Zhang, Y. & Hirakawa, K. Strong coherent energy exchange induced by the bending-bending mode-coupling effect in doubly clamped MEMS beam resonators. *Phys. Rev. Applied* **22**, 064008 (2024).

13. Ruzziconi, L., Jaber, N., Kosuru, L., Bellaredj, M. L. & Younis, M. I. Internal resonance in the higher-order modes of a MEMS beam: Experiments and global analysis. *Nonlinear Dyn.* **103**, 2197-2226 (2021).

14. Ganesan, A., Do, C. & Seshia, A. Phononic frequency comb via intrinsic three-wave mixing. *Phys. Rev. Lett.* **118**, 033903 (2017).

15. Wu, J. et al. Self-injection locked and phase offset-free micromechanical frequency combs. *Phys. Rev. Lett.* **134**, 107201 (2025).

16. Lifshitz, R. & Cross, M. C. Nonlinear dynamics of nanomechanical and micromechanical resonators. *Rev. Nonlinear Dyn. Complex.* **1**, 1 (2008).

17. Younis, M. I. *MEMS Linear and Nonlinear Statics and Dynamics* (Springer Science & Business Media, New York, 2011).

18. Kaisar, T. et al. Nonlinear stiffness and nonlinear damping in atomically thin MoS2 nanomechanical resonators. *Nano Lett.* **22**, 9831 (2022).

19. Asadi, K., Li, J., Peshin, S., Yeom, J. & Cho, H. Mechanism of geometric nonlinearity in a nonprismatic and heterogeneous microbeam resonator. *Phys. Rev. B* **96**, 115306 (2017).

20. Nayfeh, A. H. & Younis, M. I. Dynamics of MEMS resonators under superharmonic and subharmonic excitations. *J. Micromech. Microeng.* **15**, 1840 (2005).

21. Kozinsky, I., Postma, H. W. Ch., Bargatin, I. & Roukes, M. L. Tuning nonlinearity, dynamic range, and frequency of nanomechanical resonators. *Appl. Phys. Lett.* **88**, 253101 (2006).

22. Li, C., Qiu, B., Yoshioka, Y., Hirakawa, K. & Zhang, Y. Mechanical control of nonlinearity in doubly clamped MEMS beam resonators using preloaded lattice-mismatch strain. *Phys. Rev. Applied* **19**, 024025 (2023).

23. Zhang, Y. et al. Thermal tuning of mechanical nonlinearity in GaAs doubly-clamped MEMS beam resonators. *Appl. Phys. Lett.* **119**, 163503 (2021).

24. Li, Z. et al. Strain engineering of nonlinear nanoresonators from hardening to softening. *Commun. Phys.* **7**, 53 (2024).

25. Hajjaj, A. Z. & Jaber, N. Controlling resonator nonlinearities and modes through geometry optimization. *Micromachines* **12**, 1381 (2021).

26. Li, L. L. et al. Tailoring the nonlinear response of MEMS resonators using shape optimization. *Appl. Phys. Lett.* **110**, 081902 (2017).

27. Rosenberg, S., Feldman, Y. & Shoshani, O. Finding an optimal shape of a curved mechanical beam for enhanced internal resonance. *Nonlinear Dyn.* **112**, 8811 (2024).

28. Tella, S. A., Hajjaj, A. Z. & Younis, M. I. The effects of initial rise and axial loads on MEMS arches. *J. Vib. Acoust.* **139**, 040905 (2017).

Figures and captions

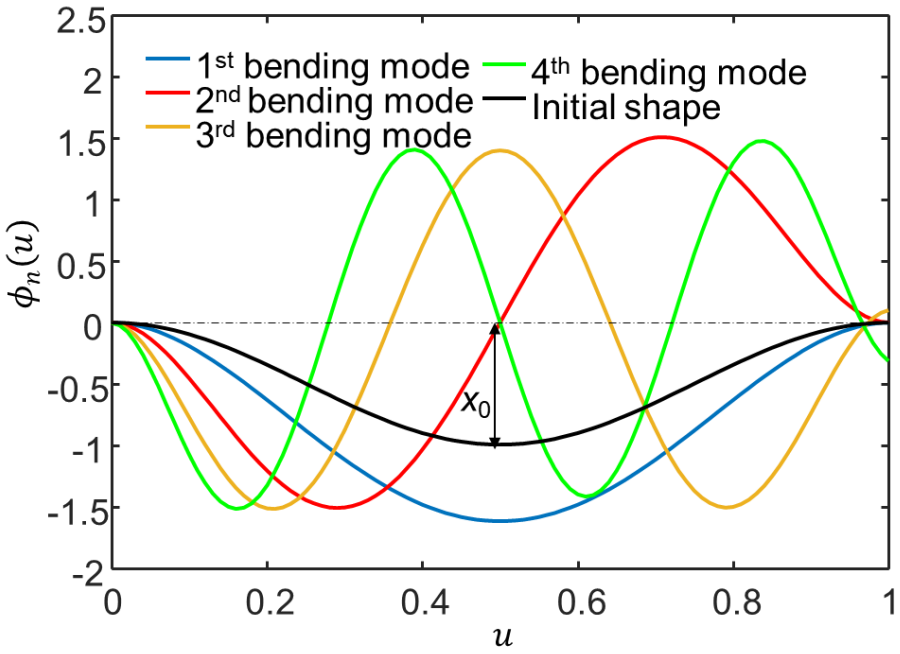

FIG. 1. One-dimensional mode shapes of the first four out-of-plane bending modes of the doubly clamped MEMS beam, together with the assumed initial beam shape. The assumed the initial shape has a center deflection of x_0. The 1st and 3rd bending modes have the same parity as the initial shape, whereas the 2nd and 4th bending modes have the opposite parity.

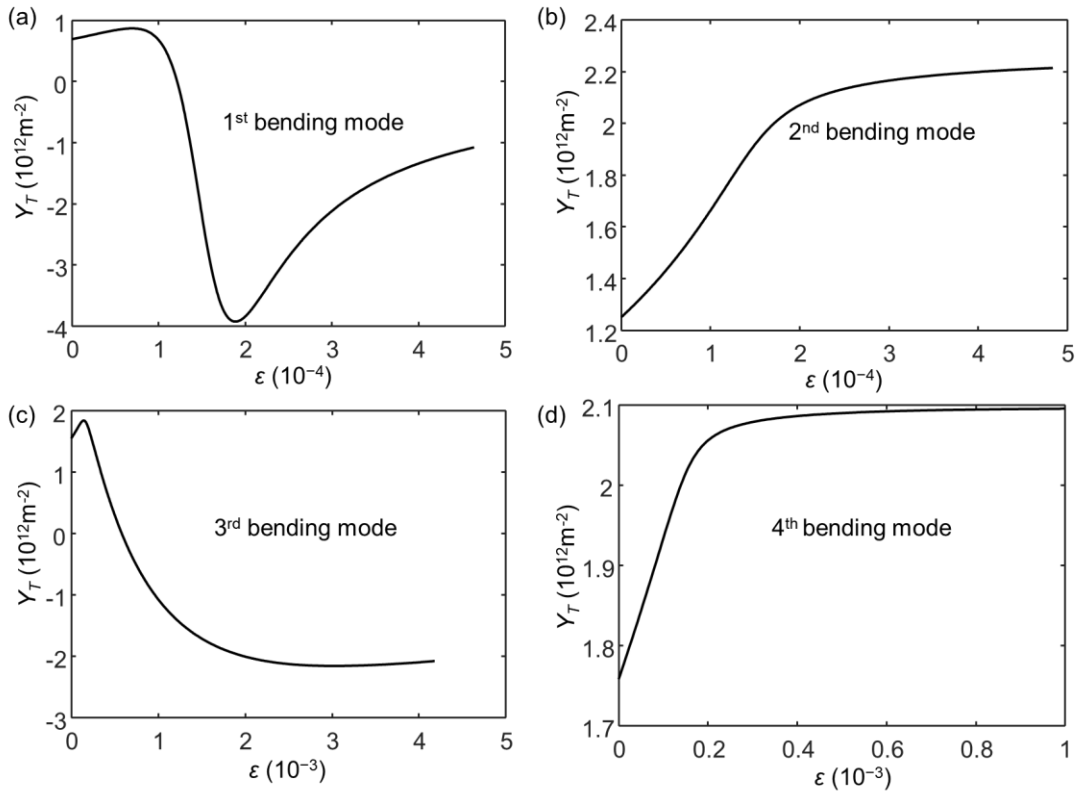

FIG. 2. Calculated total nonlinearity coefficient, Y_T, as a function of compressive strain, ε, for the present even-parity initial beam shape. Panels (a)-(d) correspond to the 1st, 2nd, 3rd, and 4th bending modes, respectively. The1st and 3rd modes, which have the same parity as the initial shape, show a transition of Y_T from positive to negative values as the compressive strain increases. In contrast, the 2nd and 4th modes, which have the opposite parity, remain in the positive Y_T over the calculated strain range.

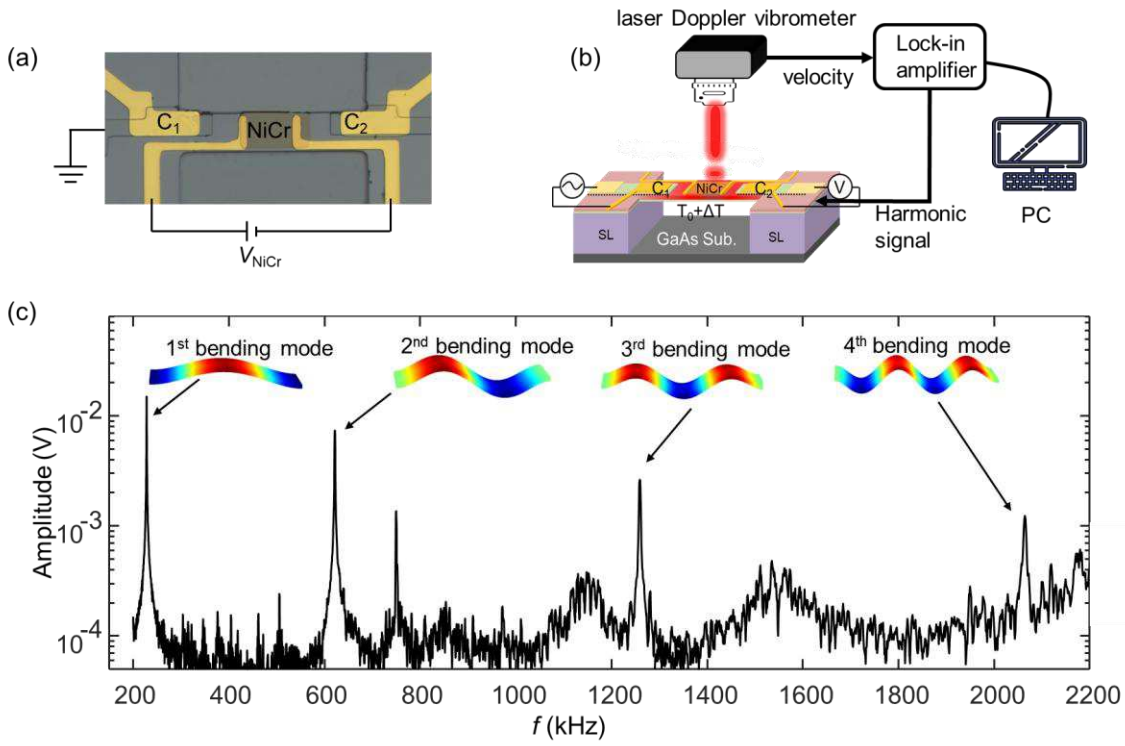

FIG. 3. Device structure and measurement configuration. (a) Microscope image of the fabricated doubly clamped MEMS beam resonator. Two piezoelectric capacitors, C_1 and C_2, are formed on the beam, and a NiCr layer is deposited at the center of the beam. A dc voltage (V_{NiCr}) is applied to the NiCr layer to generate heat in the beam. (b) Schematic illustration of the experimental setup. An ac voltage is applied to one of the piezoelectric capacitors to drive the beam, and the mechanical vibration is measured by a laser Doppler vibrometer and a lock-in amplifier with a built-in phase-locked loop. (c) Measured resonance spectrum of the first four bending modes under weak excitation. The upper insets show the corresponding mode shapes obtained by finite element modeling (FEM) simulation.

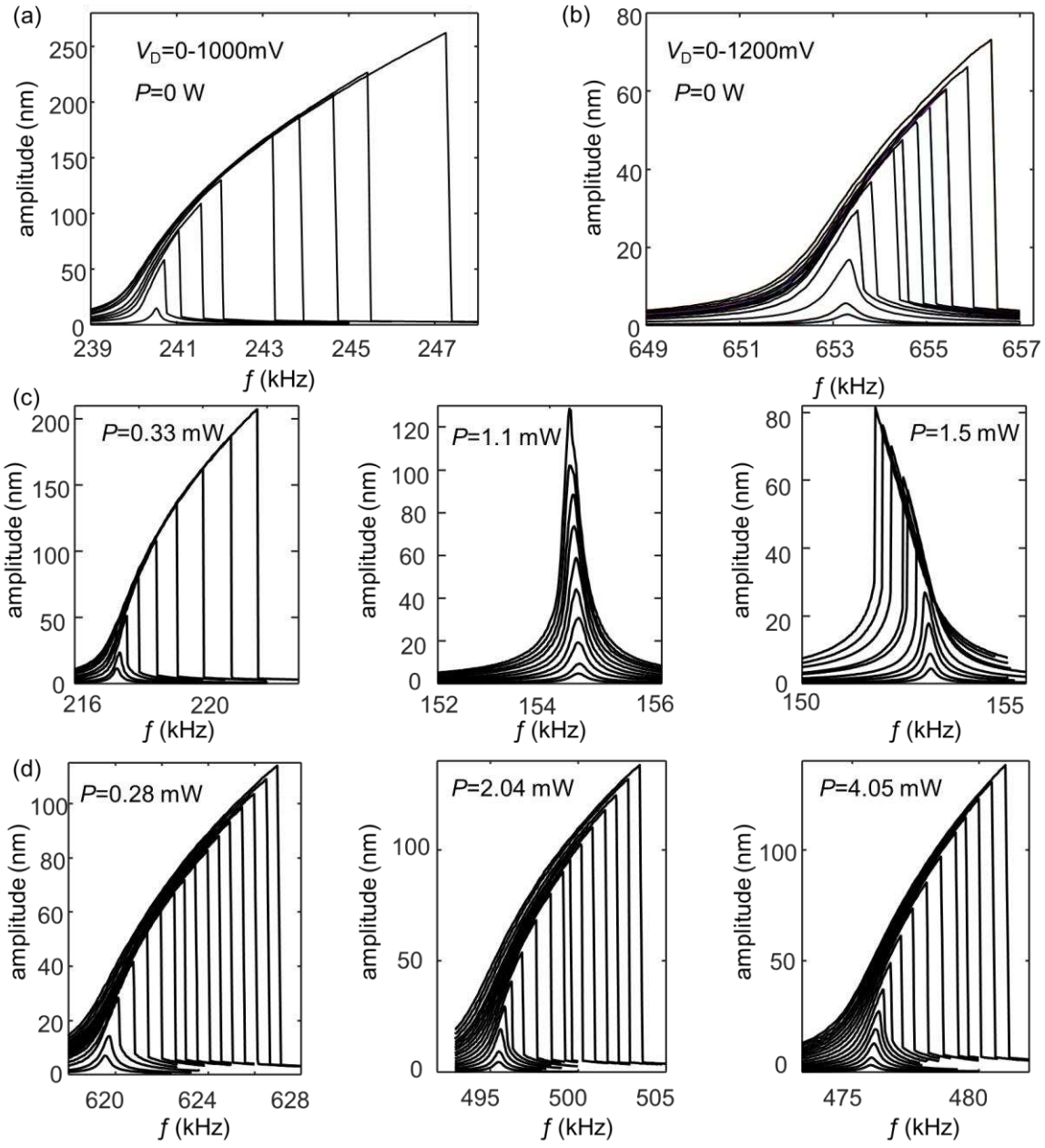

FIG. 4. Nonlinear resonance measurements and thermal tuning of the 1st and 2nd bending modes. (a), (b) Resonance spectra of the 1st and 2nd bending modes measured at different driving-voltage levels without heating, respectively. (c) Resonance spectra of the 1st bending mode under three representative heating powers. With increasing heating power, the response evolves from hardening to linear and then to softening. (d) Resonance spectra of the 2nd bending mode under

three representative heating powers. In contrast to the 1st mode, the 2nd mode mainly exhibits resonance-frequency tuning and remains in the hardening regime.

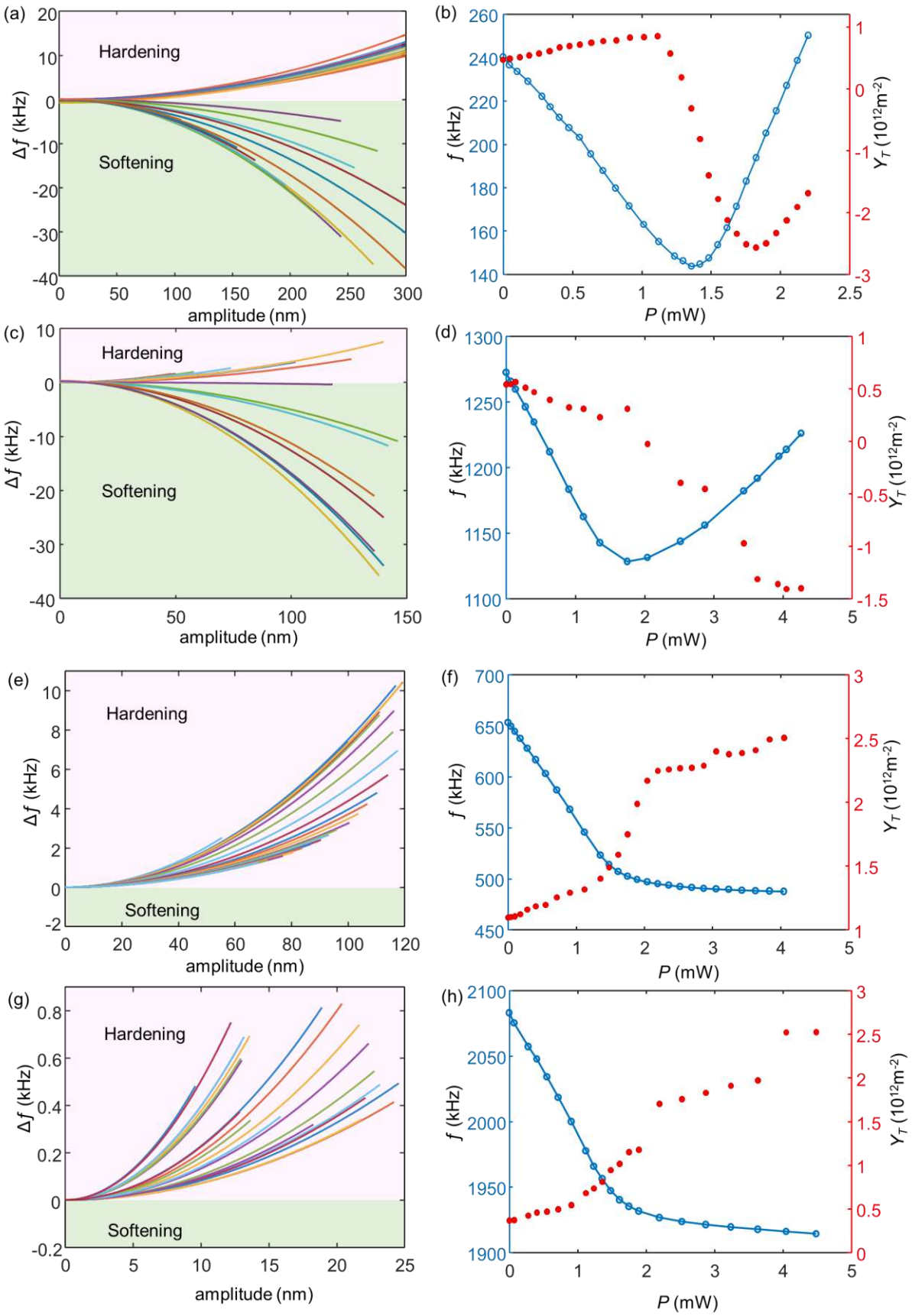
(a)
Hardening
Softening
Δf (kHz)
amplitude (nm)
(b)
f (kHz)
Y_T (10^{12}m^{-2})
P (mW)
(c)
Hardening
Softening
Δf (kHz)
amplitude (nm)
(d)
f (kHz)
Y_T (10^{12}m^{-2})
P (mW)
(e)
Hardening
Softening
Δf (kHz)
amplitude (nm)
(f)
f (kHz)
Y_T (10^{12}m^{-2})
P (mW)
(g)
Hardening
Softening
Δf (kHz)
amplitude (nm)
(h)
f (kHz)
Y_T (10^{12}m^{-2})
P (mW)

FIG. 5. Experimental verification of parity-selective tuning rule for the first four bending modes. Panels (a), (c), (e), and (g) show the measured Δf-amplitude relations at various heating powers for the 1st, 3rd, 2nd, and 4th bending modes, respectively. Panels (b), (d), (f), and (h) show the corresponding natural resonance frequency, f, and extracted total nonlinearity coefficient, Y_T, as functions of heating power, P. The 1st and 3rd modes, which have the same parity as the initial beam shape, exhibit a thermally induced sign reversal of Y_T, corresponding to a hardening-to-softening transition. The 2nd and 4th modes, which have the opposite parity, remain in the positive-Y_T over the measured heating-power range.

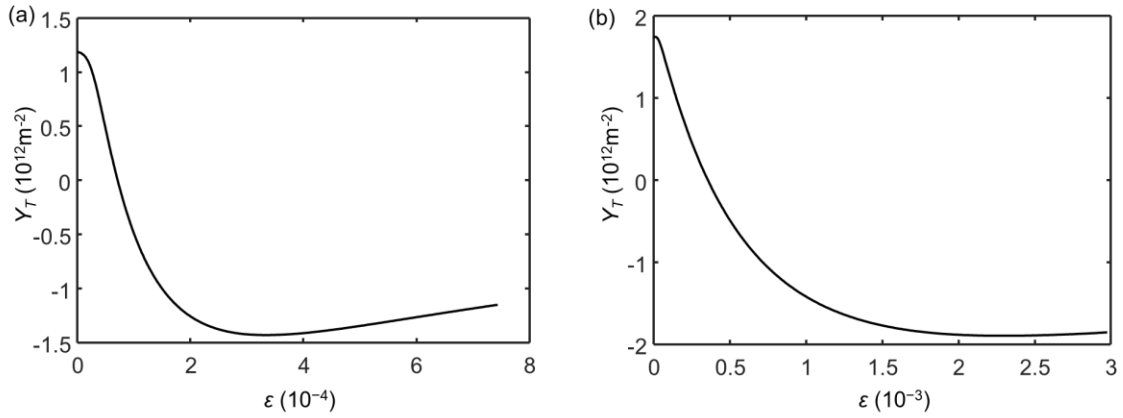

FIG. 6. Numerical results of changing the initial-shape parity. The calculated total nonlinearity coefficient, Y_T, is plotted as a function of compressive strain ε for the 2nd (a) and the 4th (b) bending modes, assuming the odd-parity initial beam shape described by Eq. (10). In contrast to the even-parity initial shape considered in Fig. 2, the odd-parity initial shape enables 2nd and 4th modes to acquire a tunable softening contribution, so that Y_T can change from positive to negative values in the calculation.